Measurement of Angular Distributions and $R = \sigma_L/\sigma_T$ in Diffractive Electroproduction of ρ^0 Mesons

The HERMES Collaboration

K. Ackerstaff[5], A. Airapetian[31], N. Akopov[31], M. Amarian[23,26,31], E.C. Aschenauer[6,12,23], H. Avakian[9,a], R. Avakian[31], A. Avetissian[31], B. Bains[14], M. Beckmann[11], S. Belostotski[25], J.E. Belz[4,27,28], Th. Benisch[8], S. Bernreuther[8], N. Bianchi[9], S. Blanchard[22], J. Blouw[23], H. Böttcher[6], A. Borissov[5,13], J. Brack[4], B. Braun[8,21], B. Bray[3], W. Brückner[13], A. Brüll[13,18], E.E.W. Bruins[18], H.J. Bulten[17,23,30], G.P. Capitani[9], P. Carter[3], E. Cisbani[26], G.R. Court[16], P.P.J. Delheij[28], E. De Sanctis[9], D. De Schepper[2,18], E. Devitsin[20], P.K.A. de Witt Huberts[23], M. Düren[8], A. Dvoredsky[3], G. Elbakian[31], J. Emerson[27,28], A. Fantoni[9], A. Fechtchenko[7], M. Ferstl[8], K. Fiedler[8], B.W. Filippone[3], H. Fischer[11], B. Fox[4], J. Franz[11], S. Frullani[26], M.-A. Funk[5], Y. Gärber[6], N.D. Gagunashvili[7], P. Galumian[1], H. Gao[2,14,18], F. Garibaldi[26], G. Gavrilov[25], P. Geiger[13], V. Gharibyan[31], A. Golendukhin[5,21,31], G. Graw[21], O. Grebeniouk[25], P.W. Green[1,28], L.G. Greeniaus[1,28], C. Grosshauser[8], A. Gute[8], V. Gyurjyan[9,b], J.P. Haas[22], W. Haeberli[17], O. Häusser[27,28,c], J.-O. Hansen[2], D. Hasch[6], R. Henderson[28], Th. Henkes[23], R. Hertenberger[21], Y. Holler[5], R.J. Holt[14], H. Ihssen[5,23], M. Iodice[26], A. Izotov[25], H.E. Jackson[2], A. Jgoun[25], C. Jones[2], R. Kaiser[6,27,28], E. Kinney[4], M. Kirsch[8], A. Kisselev[25], P. Kitching[1], K. Königsmann[11], M. Kolstein[23], H. Kolster[21], W. Korsch[3,15], V. Kozlov[20], L.H. Kramer[10,18], B. Krause[6], V.G. Krivokhijine[7], M. Kückes[28], G. Kyle[22], W. Lachnit[8], W. Lorenzon[19], A. Lung[3], N.C.R. Makins[2,14], S.I. Manaenkov[25], F.K. Martens[1], J.W. Martin[18], A. Mateos[18], K. McIlhany[3,18], R.D. McKeown[3], F. Meissner[6], F. Menden[28], D. Mercer[4], A. Metz[21], N. Meyners[5], O. Mikloukho[25], C.A. Miller[1,28], M.A. Miller[14], R. Milner[18], V. Mitsyn[7], A. Most[14,19], R. Mozzetti[9], V. Muccifora[9], A. Nagaitsev[7], Y. Naryshkin[25], A.M. Nathan[14], F. Neunreither[8], J.M. Niczyporuk[14,18], W.-D. Nowak[6], M. Nupieri[9], P. Oelwein[13], H. Ogami[29], T.G. O'Neill[2], R. Openshaw[28], J. Ouyang[28], S.F. Pate[18,22,d], M. Pitt[3], H.R. Poolman[23], S. Potashov[20], D.H. Potterveld[2], G. Rakness[4], R. Redwine[18], A.R. Reolon[9], R. Ristinen[4], K. Rith[8], G. Röper[5], H.O. Roloff[6], P. Rossi[9], M. Ruh[11], D. Ryckbosch[12], Y. Sakemi[29], I. Savin[7], K.P. Schüler[5], A. Schwind[6], T.-A. Shibata[29], T. Shin[18], A. Simon[11,22], K. Sinram[5], W.R. Smythe[4], J. Sowinski[13], M. Spengos[5], E. Steffens[8], J. Stenger[8], J. Stewart[2,16], F. Stock[8,13], U. Stösslein[6], M. Sutter[18], H. Tallini[16], S. Taroian[31], A. Terkulov[20], D.M. Thiessen[27,28], B. Tipton[18], A. Trudel[28], M. Tytgat[12], G.M. Urciuoli[26], J.F.J. van den Brand[23,30], G. van der Steenhoven[23], R. van de Vyver[12], M.C. Vetterli[27,28], M.G. Vincter[1,28], E. Volk[13], W. Wander[8,18], T.P. Welch[24], S.E. Williamson[14], T. Wise[17], K. Zapfe[5], H. Zohrabian[31]

[1] Department of Physics, University of Alberta, Edmonton, Alberta T6G 2J1, Canada[e]
[2] Physics Division, Argonne National Laboratory, Argonne, Illinois 60439-4843, USA[f]
[3] W.K. Kellogg Radiation Laboratory, California Institute of Technology, Pasadena, California 91125, USA[g]
[4] Nuclear Physics Laboratory, University of Colorado, Boulder, Colorado 80309-0446, USA[h]
[5] DESY, Deutsches Elektronen Synchrotron, 22603 Hamburg, Germany
[6] DESY Zeuthen, 15738 Zeuthen, Germany
[7] Joint Institute for Nuclear Research, 141980 Dubna, Russia
[8] Physikalisches Institut, Universität Erlangen-Nürnberg, 91058 Erlangen, Germany[i,j]
[9] Istituto Nazionale di Fisica Nucleare, Laboratori Nazionali di Frascati, 00044 Frascati, Italy
[10] Department of Physics, Florida International University, Miami, Florida 33199, USA
[11] Fakultät für Physik, Universität Freiburg, 79104 Freiburg, Germany[i]
[12] Department of Subatomic and Radiation Physics, University of Gent, 9000 Gent, Belgium[k]
[13] Max-Planck-Institut für Kernphysik, 69029 Heidelberg, Germany
[14] Department of Physics, University of Illinois, Urbana, Illinois 61801, USA[l]
[15] Department of Physics and Astronomy, University of Kentucky, Lexington, Kentucky 40506,USA
[16] Physics Department, University of Liverpool, Liverpool L69 7ZE, United Kingdom[m]
[17] Department of Physics, University of Wisconsin-Madison, Madison, Wisconsin 53706, USA[n]
[18] Laboratory for Nuclear Science, Massachusetts Institute of Technology, Cambridge, Massachusetts 02139, USA[o]
[19] Randall Laboratory of Physics, University of Michigan, Ann Arbor, Michigan 48109-1120, USA[p]
[20] Lebedev Physical Institute, 117924 Moscow, Russia
[21] Sektion Physik, Universität München, 85748 Garching, Germany[i]
[22] Department of Physics, New Mexico State University, Las Cruces, New Mexico 88003, USA[q]
[23] Nationaal Instituut voor Kernfysica en Hoge-Energiefysica (NIKHEF), 1009 DB Amsterdam, The Netherlands[r]

[24]Department of Physics, University of Oregon, Eugene, Oregon 97403, USA
[25]Petersburg Nuclear Physics Institute, St. Petersburg, Gatchina, 188350 Russia
[26]Istituto Nazionale di Fisica Nucleare, Sezione Sanità and Physics Laboratory, Istituto Superiore di Sanità, 00161 Roma, Italy
[27]Department of Physics, Simon Fraser University, Burnaby, British Columbia V5A 1S6, Canada[e]
[28]TRIUMF, Vancouver, British Columbia V6T 2A3, Canada[e]
[29]Department of Physics, Tokyo Institute of Technology, Tokyo 152, Japan[s]
[30]Department of Physics and Astronomy, Vrije Universiteit, 1081 HV Amsterdam, The Netherlands[r]
[31]Yerevan Physics Institute, 375036, Yerevan, Armenia

Abstract. Production and decay angular distributions were extracted from measurements of exclusive electroproduction of the $\rho^0(770)$ meson over a range in the virtual photon negative four-momentum squared $0.5 < Q^2 < 4$ GeV^2 and the photon-nucleon invariant mass range $3.8 < W < 6.5$ GeV. The experiment was performed with the HERMES spectrometer, using a longitudinally polarized positron beam and a ^{3}He gas target internal to the HERA e$^\pm$ storage ring. The event sample combines ρ^0 mesons produced incoherently off individual nucleons and coherently off the nucleus as a whole. The distributions in one production angle and two angles describing the $\rho^0 \to \pi^+\pi^-$ decay yielded measurements of eight elements of the spin-density matrix, including one that had not been measured before. The results are consistent with the dominance of helicity conserving amplitudes and natural parity exchange. The improved precision achieved at $4 < W < 7$ GeV, in combination with other data at $W > 7$ GeV, reveals evidence for an energy dependence in the ratio R of the longitudinal to transverse cross sections at constant Q^2.

1 Introduction

The study of exclusive photoproduction and leptoproduction of vector mesons (leaving the target nucleon(s) intact) has provided information both on the hadronic components of the photon, and on the nature of diffractive scattering. Theoretical models typically describe the exclusive production of light vector mesons as occuring via the fluctuation of the real or virtual photon into a quark-antiquark pair (or off-shell vector meson), which is scattered onto the mass shell by a diffractive interaction with the target. The corresponding tree-level diagram is shown in Fig. 1, and a list of kinematic variables describing the reaction is given in Table 1. The positron emits the virtual photon with energy ν and four-momentum squared $-Q^2$,

which then scatters from the target by the exchange of particles in the t-channel.

The decay-angle distribution is influenced by the transfer of the virtual photon's spin to that of the vector meson and can therefore provide a stringent test of the reaction mechanism. Electroproduction data are now available with modern precision in the range of the photon-nucleon centre-of-mass energy W reaching from low ($W < 4$ GeV) [1–4], through moderate ($6 < W < 20$ GeV) [5–8], and recently to very high ($50 < W < 140$ GeV) [9–11] values, and for values of Q^2 up to 30 GeV^2. A variety of competing models mentioned below have achieved some success in reproducing the observed dependences of the virtual photoproduction cross section on Q^2, W, and t. The polarization data presented here cover a range in W

Table 1. Kinematic variables used in the definition of exclusive diffractive vector meson events. (Definitions involving energies or three-vectors are given for the laboratory frame.)

Variable	Description
$k = (E, \mathbf{k})$	4-momentum of incident positron
$k' = (E', \mathbf{k'})$	4-momentum of scattered positron
$P = (M_{\mathrm{N}}, \mathbf{0})$	4-momentum of target nucleon N (ignoring Fermi motion and binding)
$q = (\nu, \mathbf{q}) = k - k'$	4-momentum of virtual photon
$q^2 = -Q^2$	Photon virtuality
$\theta_{\mathrm{e}}, \phi_{\mathrm{e}}$	Positron scattering and azimuthal angles in the lab
	($\phi_{\mathrm{e}} > 0$ defines upper half of spectrometer)
$\epsilon = (1 - \nu/E)/[1 - \nu/E + \frac{1}{2}(\nu/E)^2]$	Virtual photon polarization parameter (valid for $m_{\mathrm{e}}^2 \ll Q^2 \ll E^2$)
$W = \|(q + P)\| = (M_{\mathrm{N}}^2 + 2M_{\mathrm{N}}\nu - Q^2)^{\frac{1}{2}}$	Total photon-nucleon centre-of-mass energy
$x = Q^2/2M_{\mathrm{N}}\nu$	Bjorken scaling variable
$y = \nu/E$	Fractional leptonic energy transfer
$\mathbf{p}_{\mathrm{h}\pm}$	3-momentum of positive or negative hadron
$E_{\pi\pm} = \sqrt{m_\pi^2 + \mathbf{p}_{\mathrm{h}\pm}^2}$	Hadron energy assuming it is a pion
$p_{\mathrm{V}} = (E_{\mathrm{V}}, \mathbf{p}_{\mathrm{V}}) = (E_{\pi+} + E_{\pi-}, \mathbf{p}_{\mathrm{h}+} + \mathbf{p}_{\mathrm{h}-})$	Candidate ρ^0 4-momentum
$M_{\pi\pi} = \sqrt{p_{\mathrm{V}}^2}$	Candidate ρ^0 mass
$M_{\mathrm{Y}} = \sqrt{(P + q - p_{\mathrm{V}})^2}$	Invariant mass of the recoiling baryonic system
$t = (q - p_{\mathrm{V}})^2 < 0$	Squared 4-momentum transfer to target
t_0	Minimum of $\|t\|$ for fixed ν, Q^2, $M_{\pi\pi}$, and M_{Y}
$t' = t - t_0 < 0$	4-momentum transfer squared relative to the case
	where the meson and photon are collinear
$\Delta E = (M_{\mathrm{Y}}^2 - M_{\mathrm{N}}^2)/2M_{\mathrm{N}} = \nu - E_{\mathrm{V}} + t/2M_{\mathrm{N}}$	Measure of energy absorbed by recoil system

that fills the gap between 4 and 7 GeV containing little previous data [12], and should therefore serve as a useful additional constraint on some of these models.

The Vector Meson Dominance (VMD) model [2] has traditionally been used to describe the reaction. It treats a photon with Q^2 of order a few GeV^2 or less as a superposition of the lightest vector mesons that diffractively scatter from the target. As Q^2 increases, the hadronic content of the photon as a quark-antiquark pair is resolved. More fundamental calculations including an explicit QCD-based treatment of the dynamics of the $q\bar{q}$ pair provide a unified treatment of the entire Q^2 range for either the total [13, 14] or the longitudinal [15] cross section.
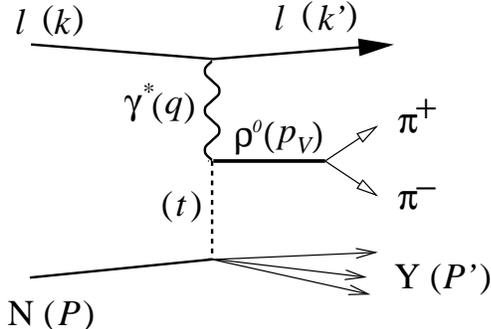

Fig. 1. Tree level diagram of diffractive vector meson electro-production viewed as two-body virtual photoproduction. Four-momentum labels are indicated in parenthesis.

In both VMD [2] and QCD-based models [14,16,17], the phenomenological Regge theory is used to describe the diffractive reaction. At low energy ($W < 4$ GeV) the process is described in terms of the exchange of mesons (ρ, ω, f_2, a_2, ω_3, ρ_3,...), all lying on the same Regge trajectory [18]. This so-called Reggeon exchange describes the decrease with W of the photoproduction cross section for real and quasi-real photons. Above $W \approx 10$ GeV, however, the cross section increases slowly, and Regge models of the reaction involve the t-channel exchange of a colorless spinless object [14,16,17], which has been identified with the soft Pomeron introduced to explain elastic pp scattering [13].

The diffractive interaction has also been treated in perturbative QCD models of longitudinal ρ^0 production, which illuminate how the Reggeons arise at a fundamental level. At the high x values corresponding to low W for moderate Q^2, the diffractive interactions arise as the result of the exchange of two quarks [19], corresponding to meson exchange in Regge theory. At low x (or high W), the interaction is assumed to involve the exchange of two gluons [15], which has led to attempts to understand the phenomenological Pomeron in terms of nonperturbative exchange of gluons [20]. At the highest Q^2, the divergence of the nucleon's gluon content at low x leads to a strong W dependence [15,17,21,22]. At the intermediate energies ($3.8 < W < 6.5$ GeV) and photon virtualities ($0.5 < Q^2 < 4$ GeV^2) available to HERMES, both the quark exchange and the gluon exchange (or, in the Regge language, both Reggeon and Pomeron exchange) processes are expected to contribute.

For unpolarized targets and polarized beams, the distribution in the production and decay angles provides information on up to 26 independent elements of the ρ^0 spin density matrix [23], providing much tighter constraints on theoretical models than the total cross section alone. Furthermore, the angular distribution yields important model-independent insight into the reaction. For example, experiments have indicated that the helicity of the photon in the $\gamma^* N$ centre-of-mass system is approximately retained by the vector meson, a phenomenon known as s-channel helicity conservation (SCHC) [2]. Given the approximate validity of SCHC, the angular distribution can be used to calculate the ratio $R \equiv \sigma_L/\sigma_T$ of longitudinal to transverse virtual-photon cross sections for exclusive ρ^0 meson production, without performing an experimentally difficult longitudinal-transverse (Rosenbluth) separation using two different beam energies. This ratio is expected to be especially sensitive to details of the theoretical models. For example, in ref. [24] it is asserted that $R(Q^2)$ is very sensitive to nonperturbative effects in the longitudinal quark-photon coupling. Recent calculations based on off-forward parton distributions have been used to describe the longitudinal cross section for exclusive ρ^0-production [19,25,26]. Some features of these models imply that in a complete QCD description higher-twist effects have to be large, a fact which should be kept in mind when interpreting the present data, especially in view of the relatively low Q^2-domain of HERMES.

Phenomenological models are often simplified by the assumption of SCHC. This assumption can be examined in calculations of spin observables including a detailed treatment of the underlying quark-gluon degrees of freedom. Violations of SCHC could arise from gluon ladders and quark loops [27]; moreover, recent models of the quark-Pomeron coupling that address issues associated with gauge-invariance lead to non-zero spin-flip amplitudes [28].

This paper reports the results from the 1995 HERMES data for the angular distribution of $\rho^0(770)$ production and decay, from which eight matrix elements related to the ρ^0 spin density matrix were extracted. Some small matrix elements that are sensitive to violations of SCHC are thereby better constrained in this energy region, including some that are accessible only using the longitudinal polarisation of the lepton beam. These data also provide the most precise determination of R in this intermediate kinematic region containing only one previous data set [12]. In combination with existing data at higher energy, these new data allow the W-dependence of R to be investigated in the region above $W = 4\,\mathrm{GeV}$, excluding the lower region where there are indications that the character of the reaction changes quickly. Below $W = 4\,\mathrm{GeV}$, the cross section increases rapidly with decreasing W, and there appears evidence of significant resonance contributions as well as a large phase difference between longitudinal and transverse production that suggests the presence of non-diffractive processes [1].

In Section 2, the experimental conditions, event selection and treatment of backgrounds are described. The representation of the general decay-angular distribution in terms of a set of matrix elements is presented in Section 3. The extraction of the matrix elements from the data is described in Section 4. The results are presented and discussed in Section 5, and the paper is summarized in Section 6.

2 Experiment

The experiment was performed using a gaseous ^{3}He target contained in an open-ended cell coaxial with the positron beam at the HERA ep collider. During 1995 HERA produced a 27.5 GeV positron beam with an average longitudinal polarization of 0.48 ± 0.03. Luminosities up to 2×10^{32} nucleons·cm^{-2}s^{-1} were achieved. Scattered positrons and coincident hadrons were detected in the HERMES spectrometer, of which a detailed description can be found elsewhere [29]. The spectrometer is equipped with front and back drift chambers before and after a 1.3 T·m dipole magnet. This tracking system provided a momentum resolution $\Delta p/p \approx 1$–2% in the 1995 running period. An iron plate that shields the circulating beams from the bending-magnet field separates the spectrometer into identically instrumented upper and lower halves. The positron trigger is produced by a timing hodoscope in coincidence with an electromagnetic calorimeter system; this system comprises a totally absorbing lead-glass array and a preshower detector consisting of a passive lead radiator and a scintillator hodoscope. This trigger required a deposit of at least 4 GeV in the lead-glass array. A gas threshold Čerenkov detector and a transition radiation detector provided additional positron/hadron separation.

2.1 Selection of Events

On-line hardware monitoring systems ensured that the only events considered were those recorded when the apparatus was fully operational. Events with exactly one identified positron and two oppositely charged hadrons were selected. Fiducial cuts were placed on the tracks to ensure that they all originated from the target and fell within the spectrometer acceptance. Positrons and hadrons were distinguished with a likelihood analysis that combined the response of the four particle-identification detectors (see [29] and references therein).

The kinematics of the detected positron define the four-momentum q and polarization parameter ϵ of the virtual photon. The kinematic constraints applied during analysis are

$$W > 3.8\,\mathrm{GeV},$$
$$Q^2 > 0.5\,\mathrm{GeV}^2,$$
$$y < 0.85,$$
$$|\sin\theta_\mathrm{e}\sin\phi_\mathrm{e}| > 0.04\,.$$

The invariant mass $M_{\pi\pi}$ of the hadron pair was reconstructed under the assumption that both hadrons were
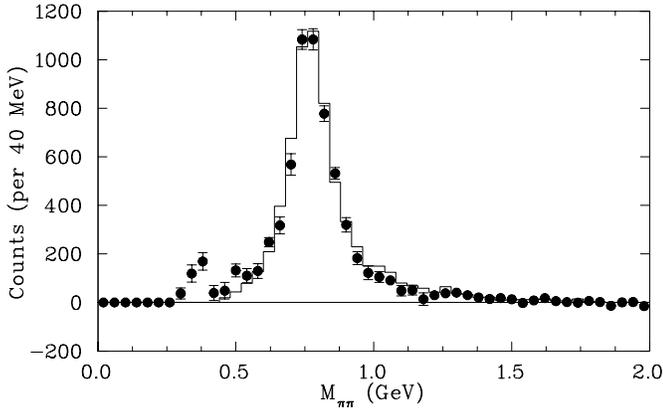
Fig. 2. $M_{\pi\pi}$ distribution for exclusive diffractive events (filled circles). The solid line is the yield from the Monte Carlo simulation, discussed in Section 4.1. The peak at low $M_{\pi\pi}$ is due to the K^+K^- decay mode of exclusively produced ϕ mesons (see section 2.2).

Fig. 3. ΔE distribution for candidate diffractive ρ^0 production events (circles), showing the exclusive peak near zero. The histogram shows the estimated contribution from non-diffractive processes (see section 2.2.1).

Fig. 4. t'-distribution for exclusive ρ^0 production events, with a fit (solid line) of (15) to the data. The contributions from coherent and incoherent scattering are shown with dashed and dotted lines, respectively.

pions (see Fig. 2). The $\rho^0(770)$ mesons were identified by the requirement

$$0.63 < M_{\pi\pi} < 0.91 \, \text{GeV}.$$

The diffractive cross section is forward peaked for small $t' \simeq -p_\perp(\rho^0)$ (see Table 1):

$$\frac{d\sigma}{dt'} \propto e^{bt'}. \tag{1}$$

Here the slope parameter b is related to the RMS radii r_ρ and r_N of the meson and nucleon or nucleus [30]:

$$b \approx \frac{1}{3}(r_\rho^2 + r_N^2). \tag{2}$$

Hence diffractive events are generally characterized by small values of t' leaving the gently recoiling target remnant well separated from the forward-going vector meson. The acceptance of the HERMES spectrometer precludes detection of the recoiling target or target remnant; however, because of the small energy width of the HERA positron beam ($\sigma_E \approx 25 \, \text{MeV}$) and the good momentum and angular resolutions of the HERMES spectrometer, the energy ΔE absorbed by the undetected target remnant can be reconstructed (see Table 1 and Fig. 3) and used to reject events in which the target nucleon(s) do not remain intact. Exclusive diffractive events were consequently selected by adding the kinematic requirements

$$\Delta E < 0.7 \, \text{GeV}, \tag{3}$$
$$-t' < 0.5 \, \text{GeV}^2.$$

Both coherent scattering from ^{3}He and incoherent scattering from nucleons are contained in the peak at $\Delta E \approx 0$, though the peaking in t' is stronger for coherent scattering because of the larger size of the ^{3}He nucleus compared with the nucleon (Fig. 4). Both contributions were included in the present analysis. The above experimental requirements were applied, to the extent applicable, in all of the results reported here, resulting in 4800 accepted events.
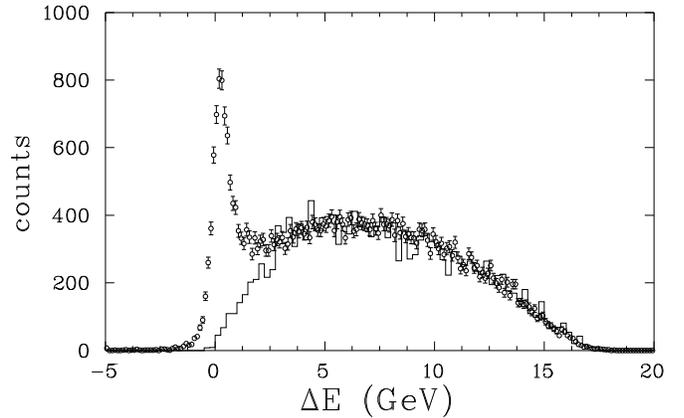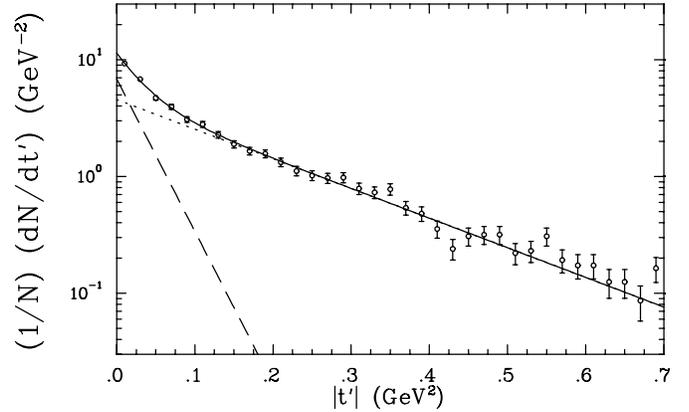
2.2 Corrections for Background

Background arises from both diffractive and non-diffractive processes. Inelastic fragmentation, *i.e.* hard scattering on partons followed by hadronization, is the primary source of non-diffractive background. The diffractive backgrounds include exclusive non-resonant $\pi^+\pi^-$ production in which the pions are produced without forming a resonance, double-diffractive dissociation in which the target remnant breaks up during diffractive vector-meson production, and exclusive production of ω mesons. The K^+K^- decay mode of the ϕ meson is reconstructed with $M_{\pi\pi}$ in the region below $0.63 \, \text{GeV}$ when pion masses are assumed for the kaons, and is thus excluded from the selected data sample. The pair production ($\gamma \to e^+e^-$) contamination of the di-hadron sample resulting from misidentification of the leptons is negligible.

2.2.1 Non-diffractive Background

Non-diffractive processes constitute the dominant source of background, for which a correction was applied using a Monte Carlo simulation. Background events were generated according to the non-diffractive deep-inelastic cross section using LEPTO, and the fragmentation was treated using the LUND model, both described in ref. [31]. The detector response was simulated with a GEANT-based Monte Carlo code [29]. Three-track $eN \rightarrow eh^+h^-X$ events were selected from these Monte Carlo events and subjected to the same analysis criteria as the data, thereby producing a sample of non-diffractive background events. The Monte Carlo estimation was normalized to the data in the inelastic region defined by $\Delta E > 4$ GeV (see Fig. 3). The experimental yields for $\Delta E < 0.7$ GeV were corrected by 6% at small Q^2 to 15% at large Q^2, using this sample of background events.

2.2.2 Diffractive Background

Measurements of double-diffractive pp scattering have suggested that the mass spectrum of the baryonic system (Y) resulting from dissociation of the target has the form [8, 32]

$$M_Y^2 \frac{d\sigma}{dM_Y^2} \propto \begin{cases} \frac{M_Y^2 - (M_N + m_\pi)^2}{1.8\,\text{GeV}^2 - (M_N + m_\pi)^2} & \text{if } M_Y^2 < 1.8\,\text{GeV}^2 \\ 1 & \text{otherwise.} \end{cases}$$

This function is shown in Fig. 5 expressed in terms of $\Delta E = (M_Y^2 - M_N^2)/2M_N$. Only 15% of diffractive events with target dissociation described by such a model would pass the ΔE cut used in this analysis, which is a benefit of the good energy resolution compared to that available in previous fixed-target leptoproduction experiments cited herein. Recent measurements of diffractive ρ^0 production with target dissociation at centre-of-mass energies from 60 GeV to 180 GeV give $\sigma_{\gamma^*p \rightarrow \rho^0 Y}/\sigma_{\gamma^*p \rightarrow \rho^0 p} = 0.65 \pm 0.17$, with a diffractive slope parameter $b_{DD} = 2.1 \pm 0.7$ GeV^{-2} [33]. Assuming that the HERMES acceptance is unaffected by target dissociation, this result implies that the contamination of the exclusive data by double-diffractive events is less than (6 ± 2)%. Moreover, no difference in the measured longitudinal fraction of ρ^0 mesons was seen between the two processes [33]. This is not surprising as target dissociation is not expected to affect the helicity structure of the $\gamma^*\rho^0$ vertex. Hence no correction or uncertainty was applied for this source of background since this contribution to the uncertainty is expected to be small compared to others.

The measured distribution includes interfering contributions from both diffractive production of $\omega(783) \rightarrow \pi^+\pi^-$ mesons (branching ratio 2.2%) and non-resonant exclusive production of $\pi^+\pi^-$ pairs, neither of which are distinguished here from diffractive ρ^0 production [34]. However, the ω production cross section is down by an order of magnitude, and its contribution tends to be cancelled by the enhancement of the background subtraction induced
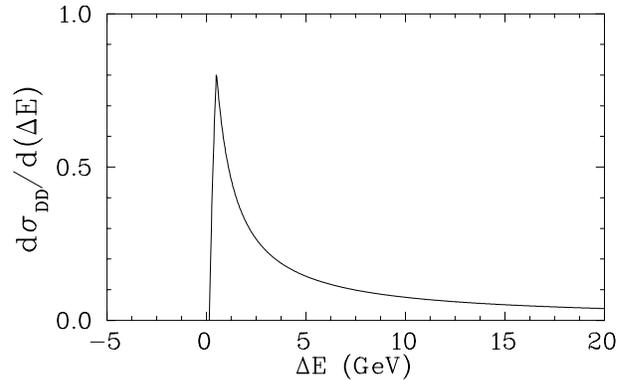

Fig. 5. A parameterization of the target excitation spectrum of double-diffractive dissociation (arbitrary units).

by the contribution to the region at larger ΔE by the dominant decay branch $\omega \rightarrow \pi^+\pi^-\pi^0$. In principle, the small non-resonant contribution should be included in any theoretical treatment that is compared to the data.

2.3 Radiative Effects

Calculated radiative corrections to the lowest order diagram (Fig. 1) have approximately a 20% effect on the measured exclusive vector meson production cross section. Radiative effects on polarization phenomena are typically much smaller. External radiative effects in the spectrometer are entirely accounted for in the GEANT-based Monte Carlo simulation. Because of the negligible target thickness and windowless cell, external bremsstrahlung before scattering is negligible. No corrections were applied for internal radiative effects; they are mitigated by the cut on ΔE (3), which ensures that no hard photon is radiated in the events used to reconstruct the production and decay angles. A systematic uncertainty was assigned for internal radiation, as discussed below.

3 Angular Distribution of the Production and Decay

3.1 The s-Channel Helicity Frame

Analyses of previous data on exclusive vector-meson production have shown that only the s-channel helicity frame leads to matrix elements that are not strongly t-dependent [35,36]. The s-channel helicity frame is the centre-of-mass system of the γ^*N system, with the quantization axis of the ρ^0 opposite to the direction of the recoiling target. The reconstructed kinematics are essentially indistinguishable for coherent and incoherent scattering, corresponding to the use of the nuclear or nucleon mass. The azimuthal production angle Φ (see Fig. 6) is defined in this frame as the angle between the lepton scattering plane and the ρ^0 production plane containing the momentum transfer to the target. The decay-angle distribution can then
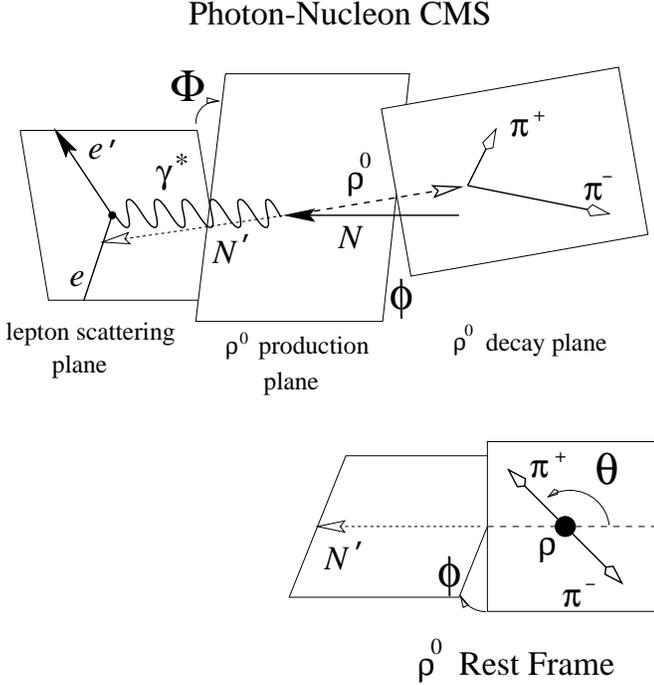
Photon-Nucleon CMS

Fig. 6. The s-channel helicity frame.

be expressed in the ρ^0 rest frame in terms of the polar and azimuthal decay angles θ and ϕ relative to the same quantization axis, with the azimuth defined relative to the vector meson production plane (see Fig. 6). The angular distribution $\mathcal{W}(\cos\theta, \phi, \Phi)$ is then completely characterized by the three angles θ, ϕ, and Φ. The spin state of the ρ^0 is reflected in the orbital angular momentum of the pion pair, giving rise to the $(\cos\theta, \phi)$ dependence. The Φ dependence of $\mathcal{W}$ arises because the virtual photon polarization depends on Φ.

3.2 Decomposition of the Angular Distribution

A complete derivation of the decay-angle distribution can be found in ref. [23]. Briefly, the decay distribution can be related to the polarization density matrix $\rho_{\lambda\lambda'}$ of the vector meson expressed in the helicity basis, using the Wigner D-functions:

$$\mathcal{W}(\cos\theta, \phi, \Phi) = \frac{3}{4\pi} \sum_{\lambda\lambda'=-1,0,1} D^{1*}_{\lambda,0}(\phi,\theta,-\phi)\rho_{\lambda\lambda'}(\Phi)D^{1}_{\lambda',0}(\phi,\theta,-\phi). \quad (4)$$

The Φ dependence appears only in $\rho_{\lambda\lambda'}$, which can be decomposed into 9 independent contributions characterized by the matrix elements $\rho^\alpha_{\lambda\lambda'}$: $\alpha = 0,1,2,3$ represent transverse photons: unpolarized, the two directions of linear polarization, and circular polarization, respectively. Pure longitudinal photons correspond to $\alpha = 4$. The remaining matrices $\alpha = 5\ldots8$ are attributable to interference of longitudinal with transverse photons. Expressions can be found in Appendix A of ref. [23] giving the various $\rho^\alpha_{\lambda\lambda'}$

in terms of combinations of the Wick amplitudes $T_{\lambda\gamma}$ for a photon of helicity γ to produce a meson of helicity λ, summed over nucleon spins.

At fixed beam energy, it is not possible to explicitly separate the contributions from longitudinal and transverse photons, and the angular distributions are described in terms of the following linear combinations of the $\rho^\alpha_{\lambda\lambda'}$:

$$r^{04}_{\lambda\lambda'} = \frac{\rho^0_{\lambda\lambda'} + \epsilon R \rho^4_{\lambda\lambda'}}{1 + \epsilon R},$$
$$r^\alpha_{\lambda\lambda'} = \frac{\rho^\alpha_{\lambda\lambda'}}{1 + \epsilon R}, \quad \alpha = (1,2,3),$$
$$r^\alpha_{\lambda\lambda'} = \sqrt{R}\frac{\rho^\alpha_{\lambda\lambda'}}{1 + \epsilon R}, \quad \alpha = (5,6,7,8).$$

Here R is the ratio of longitudinal to transverse cross sections and ϵ is the polarization parameter of the virtual photon. Equation (4) becomes [23]

$$\mathcal{W}(\cos\theta, \phi, \Phi) = \frac{3}{4\pi}\Big\{\frac{1}{2}(1 - r^{04}_{00}) + \frac{1}{2}(3r^{04}_{00} - 1)\cos^2\theta$$
$$- \sqrt{2}\,\Re(r^{04}_{10})\sin 2\theta\cos\phi - r^{04}_{1-1}\sin^2\theta\cos 2\phi$$
$$-\epsilon\cos 2\Phi\Big(r^1_{11}\sin^2\theta + r^1_{00}\cos^2\theta - \sqrt{2}\,\Re(r^1_{10})\sin 2\theta\cos\phi$$
$$- r^1_{1-1}\sin^2\theta\cos 2\phi\Big)$$
$$-\epsilon\sin 2\Phi\left(\sqrt{2}\,\Im(r^2_{10})\sin 2\theta\sin\phi + \Im(r^2_{1-1})\sin^2\theta\sin 2\phi\right)$$
$$+\sqrt{2\epsilon(1+\epsilon)}\cos\Phi\Big(r^5_{11}\sin^2\theta + r^5_{00}\cos^2\theta$$
$$- \sqrt{2}\,\Re(r^5_{10})\sin 2\theta\cos\phi - r^5_{1-1}\sin^2\theta\cos 2\phi\Big)$$
$$+\sqrt{2\epsilon(1+\epsilon)}\sin\Phi \times$$
$$\left(\sqrt{2}\,\Im(r^6_{10})\sin 2\theta\sin\phi + \Im(r^6_{1-1})\sin^2\theta\sin 2\phi\right)$$
$$+P_b\Big[\sqrt{1-\epsilon^2} \times$$
$$\left(\sqrt{2}\,\Im(r^3_{10})\sin 2\theta\sin\phi + \Im(r^3_{1-1})\sin^2\theta\sin 2\phi\right)$$
$$+\sqrt{2\epsilon(1-\epsilon)}\cos\Phi \times$$
$$\left(\sqrt{2}\,\Im(r^7_{10})\sin 2\theta\sin\phi + \Im(r^7_{1-1})\sin^2\theta\sin 2\phi\right)$$
$$+\sqrt{2\epsilon(1-\epsilon)}\sin\Phi \times$$
$$\left(r^8_{11}\sin^2\theta + r^8_{00}\cos^2\theta - \sqrt{2}\,\Re(r^8_{10})\sin 2\theta\cos\phi\right.$$
$$\left.- r^8_{1-1}\sin^2\theta\cos 2\phi\right)\Big]\Big\}, \quad (5)$$

where P_b is the longitudinal polarization of the lepton beam, and the approximation $Q^2 \gg m_e^2$ has been made.

The statistical precision of the present data set required that the analysis be limited to only one-dimensional angular distributions.

3.2.1 The $\cos\theta$ Distribution

Integrating (5) over ϕ and averaging over Φ gives

$$\mathcal{W}(\cos\theta) = \frac{3}{4}\left[1 - r^{04}_{00} + (3r^{04}_{00} - 1)\cos^2\theta\right]. \quad (6)$$

This distribution depends on only one matrix element r_{00}^{04}, which can be identified as the longitudinal fraction of ρ^0 mesons. $\mathcal{W}(\cos\theta)$ is not constrained by SCHC.

3.2.2 The ψ Distribution

The polarization angle $\psi \equiv \phi - \Phi$ is the angle between the decay plane of the ρ^0 and the plane of polarization of the photon (i.e. the lepton scattering plane). If SCHC is valid, the azimuthal dependence is a function of ψ only, and integration of (5) over $\cos\theta$ gives

$$\mathcal{W}(\psi) = \frac{1}{2\pi} \left[1 + 2\epsilon r_{1-1}^1 \cos 2\psi \right], \qquad (7)$$

which can be interpreted as an interference pattern arising from the amplitudes for production by the two linear polarization states of the photon. A positive value for r_{1-1}^1 indicates that the meson and photon spins are aligned such that decay pions are preferentially emitted in the lepton scattering plane.

3.2.3 The ϕ Distribution

Integrating (5) over $\cos\theta$ and averaging over Φ gives

$$\mathcal{W}(\phi) = \frac{1}{2\pi} \left[1 - 2r_{1-1}^{04} \cos 2\phi + P_b\sqrt{1-\epsilon^2}\, \Im(r_{1-1}^3) \sin 2\phi \right]. \quad (8)$$

The azimuthal decay angle ϕ is sensitive to the linear polarization of the ρ^0 and (4) produces only terms of the form $e^{i(\lambda-\lambda')\phi}$ with $|\lambda - \lambda'| = 2$. This distribution measures any SCHC-violating couplings of the linear polarization $(\lambda = 1, \lambda' = -1)$ of the vector meson to transverse unpolarized $(\alpha = 0)$ and circularly polarized $(\alpha = 3)$, and longitudinal $(\alpha = 4)$ photons. If SCHC holds, then $\mathcal{W}(\phi) = 1/2\pi$.

3.2.4 The Φ Distribution

Integration of $\mathcal{W}(\cos\theta, \phi, \Phi)$ over $\cos\theta$ and averaging over ϕ is equivalent to summing over the final state helicities (λ, λ'), giving

$$\mathcal{W}(\Phi) = \frac{1}{2\pi} \left\{ 1 - \epsilon \cos 2\Phi \operatorname{Tr}(r^1) + \sqrt{2\epsilon(1+\epsilon)} \cos\Phi \operatorname{Tr}(r^5) \right.$$
$$\left. + P_b\sqrt{2\epsilon(1-\epsilon)} \sin\Phi \operatorname{Tr}(r^8) \right\}. \qquad (9)$$

As a sum over the ρ^0 decay states, $\mathcal{W}(\Phi)$ measures the out-of-plane dependence of the $eN \to eN\rho^0$ reaction, and the matrix elements $\operatorname{Tr}(r^1)$, $\operatorname{Tr}(r^5)$, and $\operatorname{Tr}(r^8)$ can be identified with the out-of-plane response functions familiar from medium-energy quasi-elastic electron scattering: W_{TT}, W_{LT}, and $W_{LT'}$, respectively (see [37]). Parity conservation ensures that $r_{11}^\alpha = r_{-1-1}^\alpha$, for $\alpha = 0, 1, 4, 5, 8$; thus $\operatorname{Tr}(r^\alpha) = 2r_{11}^\alpha + r_{00}^\alpha$, in agreement with the notation of ref. [23]. If SCHC applies, then $\mathcal{W}(\Phi) = 1/2\pi$.

4 Extraction of Matrix Elements

To account for radiative and instrumental effects on the measurements, a Monte Carlo event generator for exclusive diffractive ρ^0 production was developed and used in conjunction with the GEANT detector simulation. The matrix elements were extracted as those values that best fitted the Monte Carlo distributions to the data.

4.1 Monte Carlo Event Generator

The diffractive ρ^0 generator produces $eN \to eN\rho^0$ events according to the leptoproduction double-differential cross section [2]

$$\frac{d\sigma}{dQ^2 dE'} = \frac{1}{4\pi E E'} \Gamma_T(Q^2, E') \sigma(Q^2), \qquad (10)$$

where the virtual photon flux is defined according to the Hand convention [38]

$$\Gamma_T(Q^2, E') = \frac{\alpha}{4\pi^2} \frac{W^2 - M_N^2}{2M_N} \frac{1}{Q^2} \frac{E'}{E} \frac{2}{1-\epsilon}. \qquad (11)$$

Using VMD, the virtual photon production cross section can be expressed in terms of the real photoproduction cross section as [2,4]

$$\sigma(Q^2) = \frac{1}{(1 + Q^2/M_\rho^2)^2} \cdot \sigma(Q^2 = 0), \qquad (12)$$

$$\sigma(Q^2 = 0) = A_\gamma \frac{2M_P}{W^2 - M_P^2} + B_\gamma, \qquad (13)$$

with $A_\gamma = 29.4\,\mu\mathrm{b} \cdot \mathrm{GeV}$ and $B_\gamma = 9.5\,\mu\mathrm{b}$ from a fit to data from ref. [4].

The ρ^0 mass selection was weighted according to a skewed Breit-Wigner distribution

$$\frac{dN}{dM_{\pi\pi}} = \frac{M_{\pi\pi}\Gamma_\rho M_\rho}{(M_{\pi\pi}^2 - M_\rho^2)^2 + M_\rho^2\Gamma_\rho^2} \left(\frac{M_\rho}{M_{\pi\pi}} \right)^{n_s}. \qquad (14)$$

The mass-dependent width $\Gamma_\rho(M_{\pi\pi})$ and skewing parameter $n_S = 3.18$ were taken from ref. [39].

The events were generated from an exponential distribution in t', and weighted to account for the coherent contribution at low t':

$$\frac{dN}{dt'} \propto \frac{\sigma_A}{\sigma_N} b_A e^{b_A t'} + b_N e^{b_N t'}. \qquad (15)$$

The ratio of the total coherent cross section from ^{3}He to the incoherent one from nucleons was set to $\sigma_A/\sigma_N = 0.48$, and the diffractive slope for ^{3}He (the nucleon) was taken as $25\,(6)\,\mathrm{GeV}^{-2}$ (e.g. see [2]). The present data set was found to be consistent with (12–15) using the parameters as given above. While the value of the skewing parameter $n_S = 3.0\pm0.02$ provides a better fit [40], this hardly affects the angular distributions.

4.2 Procedure

The analysis was done in four Q^2 regions containing data of approximately equal statistical precision: $0.5 \ldots 0.95 \ldots 1.3 \ldots 1.96 \ldots 4$ GeV^2. For each Q^2 bin, a sample of Monte Carlo events was generated from a distribution that is isotropic in all angles. These events were then subjected to the simulation of the experiment and normal data analysis procedures, accounting for the rather severe effects of the spectrometer acceptance. In order to impose the effects of the $r_{\lambda\lambda'}^\alpha$ on the shapes of the simulated angular distributions, the surviving $N_{MC} \approx 1.5 \times 10^4$ events were weighted according to

$$w_i = \mathcal{W}(\cos\theta_i, \phi_i, \Phi_i; \epsilon_i) \quad (i = 1, ..., N_{MC}),$$

with $\mathcal{W}(\cos\theta_i, \phi_i, \Phi_i; \epsilon_i)$ given by (5). The $\cos\theta_i$, ϕ_i, Φ_i, and ϵ_i refer to the generated kinematics of each Monte Carlo event. The weights w_i were evaluated as a function of the 23 r-matrix elements describing $\mathcal{W}(\cos\theta, \phi, \Phi)$ (5) as follows:

- The matrix elements that control the one-dimensional distributions $\mathcal{W}(\cos\theta)$, $\mathcal{W}(\phi)$, $\mathcal{W}(\Phi)$, and $\mathcal{W}(\psi)$, were taken as free parameters: r_{00}^{04}, r_{1-1}^{04}, r_{1-1}^1, r_{1-1}^3, Tr(r^1), Tr(r^5) and Tr(r^8).
- An eighth free parameter was taken to be the phase δ between the longitudinal and transverse Wick amplitudes T_{00} and T_{11} — the only ones remaining under the assumption of SCHC and natural parity exchange [23]. This parameter was used to constrain the following matrix elements:

$$-\Im(r_{10}^6) = \Re(r_{10}^5) \equiv \frac{1}{2}\sqrt{\frac{R}{2}}\frac{\cos\delta}{(1+\epsilon R)}, \qquad (16)$$

$$\Im(r_{10}^7) = \Re(r_{10}^8) \equiv \frac{1}{2}\sqrt{\frac{R}{2}}\frac{\sin\delta}{(1+\epsilon R)}, \qquad (17)$$

with R calculated from r_{00}^{04} and ϵ according to (21). The $r_{10}^{5,6,7,8}$ terms, due to longitudinal-transverse interference, cause a correlation between $\cos\theta$ and ψ and are not observable in one-dimensional angular distributions; however, the correlation between $\cos\theta$ and ϕ in the detector acceptance function caused by the intrusion of the magnet shielding plate requires that all matrix elements must be fitted simultaneously.
- The matrix elements describing the azimuthal production angle (Φ) distribution were assumed to have the helicity structure

$$r_{00}^{1,5,8} = \text{Tr}(r^{1,5,8})\,r_{00}^{04}, \qquad (18)$$

$$r_{11}^{1,5,8} = \text{Tr}(r^{1,5,8})\,\frac{1}{2}(1 - r_{00}^{04}), \qquad (19)$$

which assigns to these amplitudes the same ratio of longitudinal-to-transverse strength as observed in the distribution averaged over Φ.
- The remaining matrix elements are not observable in the one-dimensional distributions and were constrained

assuming SCHC [23] by

$$\Im(r_{1-1}^2) = -r_{1-1}^1,$$
$$r_{1-1}^{5,6,7,8} = 0,$$
$$r_{10}^{1,2,3,04} = 0.$$

The 8 free parameters plus a single arbitrary global normalization factor were simultaneously adjusted to minimize the total χ^2 of the deviations between the data and the Monte Carlo model in their reconstructed yield distributions $dN/d\cos\theta$, $dN/d\phi$, $dN/d\Phi$, and $dN/d\psi$. The χ^2 per degree of freedom ranges from 29/42 to 48/42 for the four Q^2 bins. The optimized parameters and their uncertainties are taken to be the measured values at each Q^2 point. The quoted statistical uncertainties include the effects of the significant correlations between parameters.

4.3 Systematic Uncertainties

Systematic uncertainties due to assumptions used in the analysis were estimated by performing the analysis under different yet tenable assumptions and comparing results. The following issues were investigated:

- Geometric acceptance: The systematic uncertainty due to alignment errors was estimated by varying the alignment in the GEANT model within known tolerances and performing the analysis procedure on Monte Carlo data. This contribution tends to dominate at small Q^2 for all matrix elements except Tr(r^1) and Tr(r^8).
- Assumptions in the VMD-based diffractive generator: Q^2 and W dependence ((12) and (13)), relative contributions (σ_A/σ_N) from coherent and incoherent scattering and the diffractive slope parameters b_N and b_A (15) were all varied within uncertainties.
- Background correction: The systematic uncertainty attributable to the background correction was estimated by varying the ΔE cut in the analysis procedure.
- Relative contributions of $r_{00}^{1,5,8}$ and $r_{11}^{1,5,8}$ to the trace Tr$(r^{1,5,8})$ ((18) and (19)) measured by the $\mathcal{W}(\Phi)$ distribution (9).
- Possible violations of SCHC: Previous measurements [1, 5] covering a wide energy range have yielded non-zero values for r_{10}^{04}, which can be attributed to interference between a small spin-flip amplitude and a non-spin-flip amplitude $|T_{\text{flip}}|/|T_{\text{no-flip}}| \approx 0.14$ (see Appendix 1 of Ref. [1]).
- Radiative effects: The spectrometer material in the path of the scattered positrons leaving the target is about 5% of a radiation length. This happens to be an amount that will produce an effect similar to that of internal radiation, based on the equivalent radiator approximation [41]. Hence the systematic uncertainty attributable to uncorrected internal radiative effects was estimated by comparing fit results using Monte Carlo data generated with and without external radiative effects.

The uncertainty contributions thus estimated were added in quadrature.
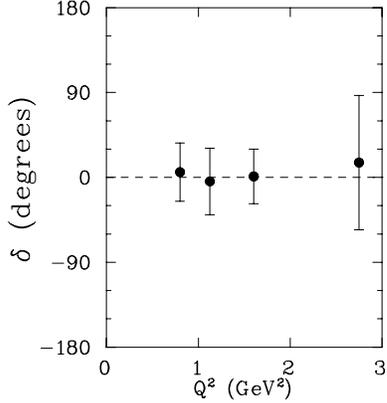
Fig. 7. Best-fit values for the phase difference δ between the longitudinal and transverse amplitudes (statistical uncertainties only).

5 Results and Discussion

The best-fit values of the phase angle δ shown in Fig. 7 are consistent with zero, as previously observed for $W > 3\,\mathrm{GeV}$ [2], and as expected when both longitudinal and transverse production are diffractive.

Previous data have typically been presented as one-dimensional distributions with corrections for instrumental effects applied. In keeping with this tradition, an acceptance correction was trivially obtained from the optimized matrix elements by comparing the Monte Carlo yields ($dN/d\cos\theta$, $dN/d\phi$, $dN/d\Phi$, and $dN/d\psi$) with the analytic expressions (6–7) for the angular distributions ($\mathcal{W}(\cos\theta)$, $\mathcal{W}(\phi)$, $\mathcal{W}(\Phi)$, and $\mathcal{W}(\psi)$, respectively). The corresponding measured angular distributions after applying this correction are shown for four values of Q^2 in Figs. 8, 11, 13 and 9. These figures should be interpreted with caution, as each one alone does not adequately represent the global fit involving strong correlations between the resulting matrix elements. Systematic and statistical uncertainties combined in the error bands apply in the same way to both the curves representing the results of the global fit and — through the acceptance correction — the data.

5.1 Matrix Elements Allowed by SCHC

As observed in previous measurements, the $\mathcal{W}(\cos\theta)$ distribution in Fig. 8 shows a dramatic shift as Q^2 increases, from a predominantly $\sin^2\theta$ shape to a predominantly $\cos^2\theta$ shape, indicating a transition from transverse to longitudinal production (see (6)). The structure of $\mathcal{W}(\psi)$ visible in Fig. 9 is entirely due to transverse ρ^0 mesons (r^1_{1-1} in (7)), so that as the longitudinal component increases, the 'damping' of the $\mathcal{W}(\psi)$ distribution indicates a complementary decrease in r^1_{1-1} because of the dilution from longitudinal ρ^0 mesons. The measured matrix elements r^{04}_{00} and r^1_{1-1} are plotted versus Q^2 in Fig. 10 and are listed in Table 2. Comparison with data of other experiments in Fig. 10 is complicated by their different values

of the polarization parameter ϵ. For that reason, this issue will be revisited when discussing the values of R derived from the data in Fig. 10.

If SCHC is valid and the $\gamma^*N \to \rho^0 N$ reaction proceeds via the t-channel exchange of a particle with natural parity ($\mathrm{J}^P = 0^+, 1^-,...$), then the tensor alignment of the mesons in the scattering plane is related to the transverse fraction of mesons by

$$2r^1_{1-1} = (1 - r^{04}_{00}). \tag{20}$$

Thus the decay pions from transverse ρ^0 mesons are preferentially emitted in the scattering plane, while those emitted from longitudinal ρ^0 mesons show no ψ dependence. A comparison of the last two columns of Table 2 reveals that the measured values of r^{04}_{00} and r^1_{1-1} are in excellent agreement with (20), with a total χ^2 of 2.7 for 4 degrees of freedom, accounting for correlations. This demonstrates that the reaction is dominated by helicity-conserving amplitudes with natural parity exchange.

5.2 Matrix Elements forbidden by SCHC

The distributions in the azimuthal decay and production angles ϕ and Φ are shown in Figs. 11 and 13; the matrix elements describing the distributions can be found in Tables 3 and 4 respectively, and are plotted versus Q^2 in Figs. 12 and 14. Where other data exist, they are consistent. The present data for $\mathrm{Tr}(r^1)$ and $\mathrm{Tr}(r^5)$ interpolate in Q^2 between the photo- and lepto-production data from the collider experiments [10,11], but appear consistent in spite of the large difference in W. No previous data for $\mathrm{Tr}(r^8)$ exist. The extraction of $\Im(r^3_{1-1})$ and $\mathrm{Tr}(r^8)$ depends on the use of a polarized lepton beam. Even though a single beam helicity was used, the effect of the term involving r^3_{1-1} is not visible, and only a $\cos 2\phi$ variation can be seen in $\mathcal{W}(\phi)$. This dependence is clearly visible in Fig. 11 at the smallest value of Q^2, although this variation has only marginal significance in comparison with the total uncertainties. Within the systematic uncertainty of the measurement, the present results are in fair agreement with the SCHC prediction that $r^{04}_{1-1} = \Im(r^3_{1-1}) = \mathrm{Tr}(r^1) = \mathrm{Tr}(r^5) = \mathrm{Tr}(r^8) \equiv 0$, though small negative values for r^{04}_{1-1} and $\mathrm{Tr}(r^1)$ (for the latter 1.8 standard deviations at the smallest Q^2, and about 2.5 σ averaged over Q^2) could both be attributed to the interference of a small double-spin-flip amplitude with a non-spin-flip amplitude. Similarly, the non-zero value of $\mathrm{Tr}(r^5)$ — 3.5 standard deviations averaged over Q^2, ignoring the systematic uncertainties which only in this case are dominated by radiative effects — could be caused by interference of a spin-flip amplitude with a helicity conserving amplitude (see Appendix A of [23] and Appendix 1 of [1]). The present data are in agreement with the significantly positive values for $\mathrm{Tr}(r^5)$ from the HERA colliding-beam experiments at large W, which reflect the similar SCHC-violating behaviour reported for their values of r^5_{00} [10,11]. However, radiative effects are not included in their systematic uncertainties. This violation by r^5_{00} was not observed in measurements with apparently similar precision at low $W (\sim 2.3\,\mathrm{GeV})$ [1].
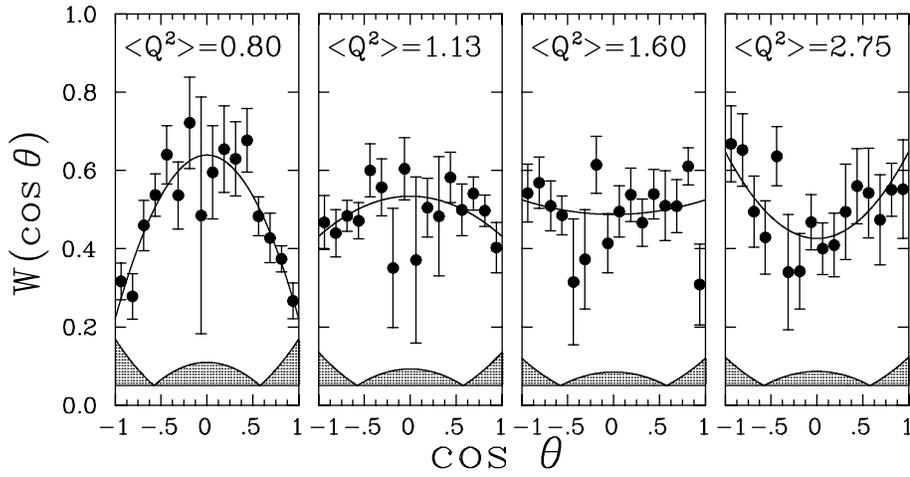
Fig. 8. The acceptance-corrected angular distributions $\mathcal{W}(\cos\theta)$ in four regions of Q^2, with statistical error bars. The solid curves are from (6) evaluated with the best-fit matrix elements. The shaded regions indicate the uncertainty of the curves (or of the acceptance correction to the points) arising from the total uncertainty of r_{00}^{04} (see text). The average values of Q^2 are shown in GeV^2.
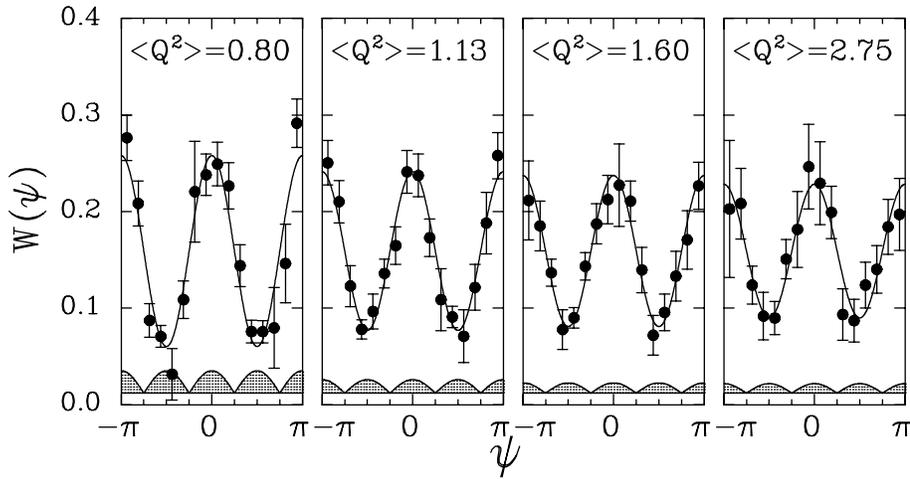

Fig. 9. The acceptance-corrected angular distributions $\mathcal{W}(\psi)$ in four regions of Q^2, with statistical error bars. The solid curves are from (7) evaluated with the best-fit matrix elements. The shaded regions indicate the uncertainty of the curves arising from the total uncertainty of r_{1-1}^1. The average values of Q^2 are shown in GeV^2.
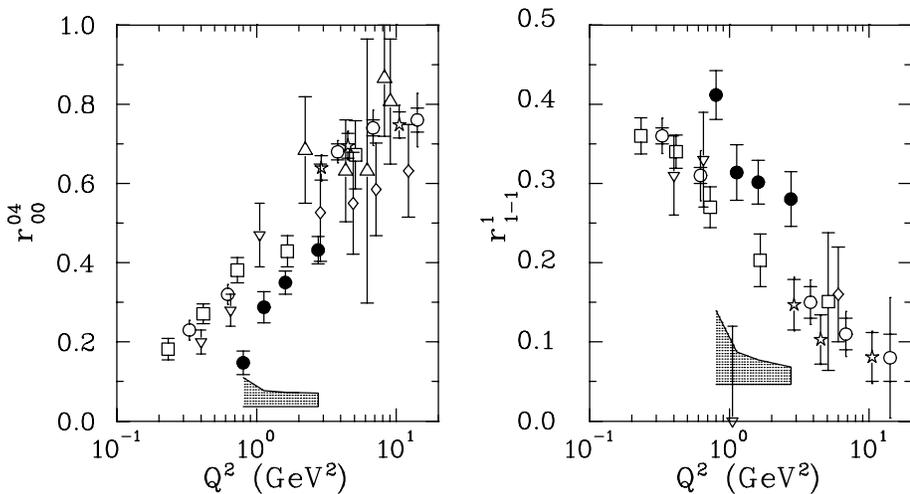

Fig. 10. The spin density matrix elements r_{00}^{04} and r_{1-1}^1 as a function of Q^2 ($\bullet$), with the band representing the systematic uncertainty. There are shown for comparison previous measurements with statistical uncertainties as (inner) error bars, from DESY [1] (∇), EMC [6] ($\triangle$), NMC [7] ($\diamond$), E665 [8] ($\square$), ZEUS [9] ($\circ$), and H1 [11] ($\star$). Where the systematic uncertainties were specified [9,11], they are added in quadrature to produce the outer error bars.

$\langle Q^2\rangle$ (GeV^2)	$\langle\epsilon\rangle$	measured r_{00}^{04}	measured r_{1-1}^1	r_{1-1}^1(SCHC) from r_{00}^{04}
0.80	0.76	$0.147 \pm 0.030 \pm 0.073$	$0.412 \pm 0.031 \pm 0.093$	0.43 ± 0.02
1.13	0.82	$0.288 \pm 0.040 \pm 0.041$	$0.314 \pm 0.035 \pm 0.041$	0.36 ± 0.02
1.60	0.81	$0.350 \pm 0.029 \pm 0.036$	$0.302 \pm 0.028 \pm 0.031$	0.32 ± 0.02
2.75	0.78	$0.432 \pm 0.035 \pm 0.034$	$0.280 \pm 0.034 \pm 0.022$	0.28 ± 0.02

Table 2. Spin density matrix elements describing the distributions in decay angle $\mathcal{W}(\cos\theta)$ and in polarization angle $\mathcal{W}(\psi)$. The measured values of r_{1-1}^1 are compared with the predictions based on (20) using the measured values of r_{00}^{04}. The first (second) uncertainty is statistical (systematic).
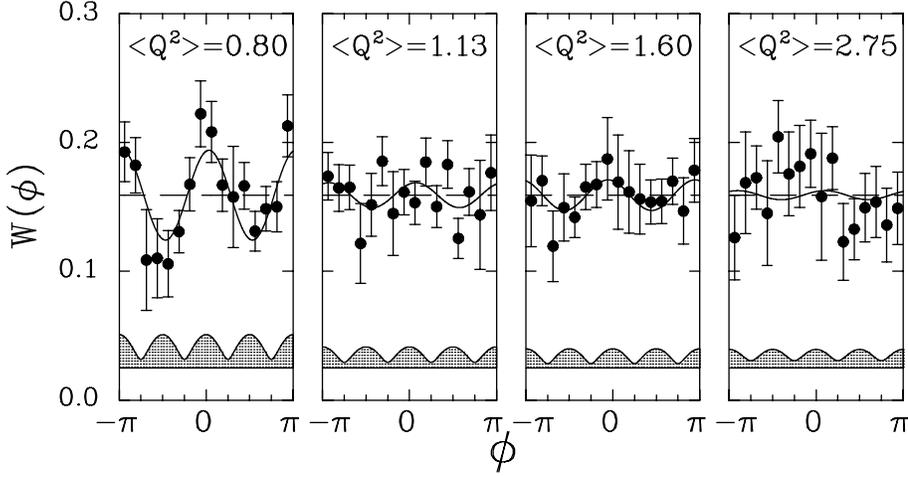
Fig. 11. The acceptance-corrected angular distributions $\mathcal{W}(\phi)$ in four regions of Q^2, with statistical error bars. The solid curves are from (8) evaluated with the best-fit matrix elements. The shaded regions indicate the uncertainty of the curves arising from the total uncertainties in r_{1-1}^{04} and $\Im(r_{1-1}^3)$. The average values of Q^2 are shown in GeV^2. The dashed horizontal line represents the value $\frac{1}{2\pi}$ predicted by SCHC.
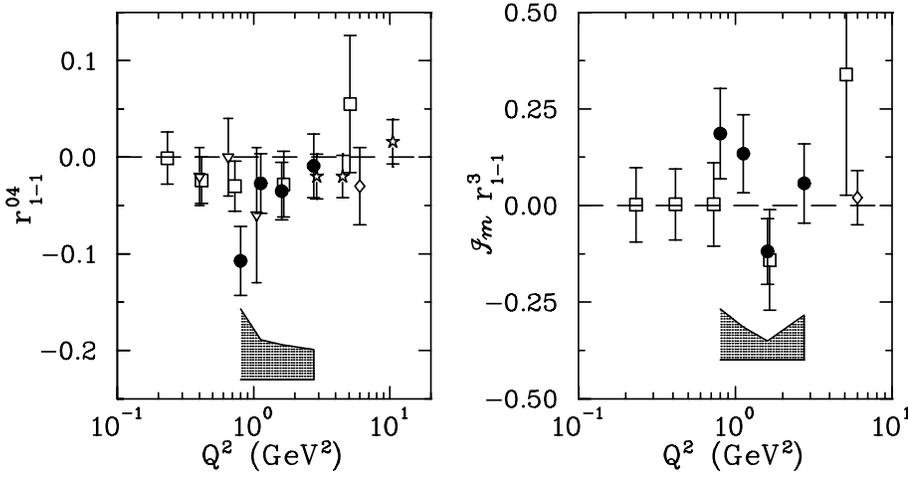

Fig. 12. The spin density matrix elements for r_{1-1}^{04} and $\Im(r_{1-1}^3)$ as a function of Q^2 ($\bullet$), with the band representing the systematic uncertainty. There are shown for comparison previous measurements with statistical uncertainties only from DESY [1] ($\triangledown$), NMC [7] ($\diamond$), E665 [8] ($\square$), and from H1 [11] ($\star$) where the systematic uncertainties are specified to be negligible in this case.

$\langle Q^2\rangle$ (GeV^2)	$\langle\epsilon\rangle$	r_{1-1}^{04}	$\Im(r_{1-1}^3)$
0.80	0.76	$-0.107 \pm 0.036 \pm 0.073$	$0.186 \pm 0.117 \pm 0.132$
1.13	0.82	$-0.027 \pm 0.031 \pm 0.041$	$0.134 \pm 0.101 \pm 0.086$
1.60	0.81	$-0.035 \pm 0.030 \pm 0.036$	$-0.119 \pm 0.085 \pm 0.049$
2.75	0.78	$-0.009 \pm 0.033 \pm 0.034$	$0.057 \pm 0.103 \pm 0.116$

Table 3. Spin density matrix elements describing the the azimuthal decay-angle distribution $\mathcal{W}(\phi)$. The first (second) uncertainty is statistical (systematic).

5.3 Ratio of Longitudinal to Transverse Cross Sections

With the assumption of s-channel helicity conservation, knowledge of the virtual photon polarization allows extraction of the ratio of the longitudinal to transverse cross sections for diffractive ρ^0 production

$$R \equiv \frac{\sigma_L}{\sigma_T} = \frac{1}{\epsilon} \frac{r_{00}^{04}}{1 - r_{00}^{04}} \tag{21}$$

without having to combine data at different beam energies. The right side of (21) can be interpreted simply as the fraction r_{00}^{04} of longitudinal ρ^0 mesons normalized to the fraction ϵ of longitudinal photons, divided by the fraction $(1 - r_{00}^{04})$ of transverse ρ^0 mesons normalized to the unit flux of transverse photons.

As r_{00}^{04} in (21) depends only on the squares of amplitudes, (21) is robust against SCHC violations. For in-

stance, the SCHC-violating spin-flip amplitudes reported in [1,5] to be as large as 14% of the SCHC-conserving non-spin-flip amplitude require only a 2% correction after squaring them. Moreover, the double-spin-flip amplitudes T_{-11} and T_{1-1} couple transverse $m = \pm 1$ photons to $m = \mp 1$ ρ^0 mesons, and therefore do not affect the validity of (21).

Equation (21) was used to determine R; the results are listed in Table 5, and plotted in Fig. 15 together with previous data with relevant precision in the regime $W > 4\,\text{GeV}$. Gauge invariance restricts R to be zero at $Q^2 = 0$, and dimensional arguments imply that the longitudinal cross section dominates at asymptotically large Q^2 [15]. All of the sets of existing data are consistent with a monotonic interpolation between these extremes, and show that both the transverse and longitudinal production mecha-
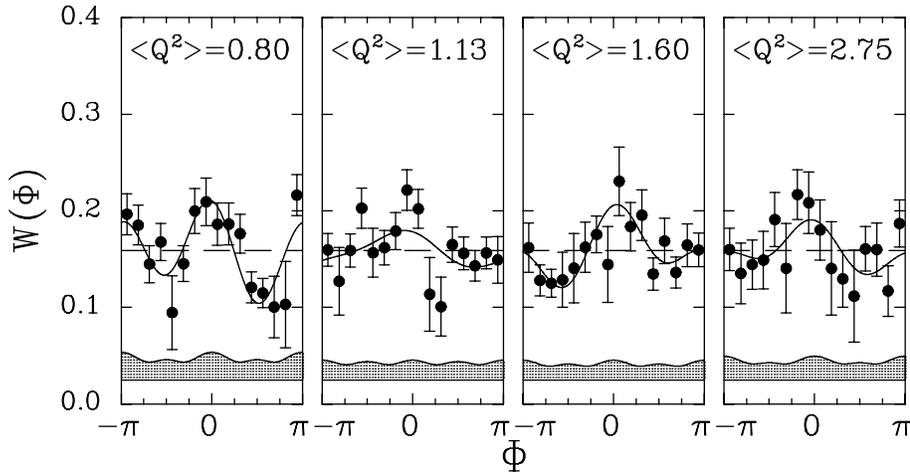
Fig. 13. The acceptance-corrected angular distributions $\mathcal{W}(\Phi)$ in four regions of Q^2, with statistical error bars. The solid curves are from (9) evaluated with the best-fit matrix elements. The shaded regions indicate the uncertainty of the curves arising from the total uncertainties in $\mathrm{Tr}(r^1)$, $\mathrm{Tr}(r^5)$, and $\mathrm{Tr}(r^8)$. The average values of Q^2 are shown in GeV^2. The dashed horizontal line represents the value $\frac{1}{2\pi}$ predicted by SCHC.
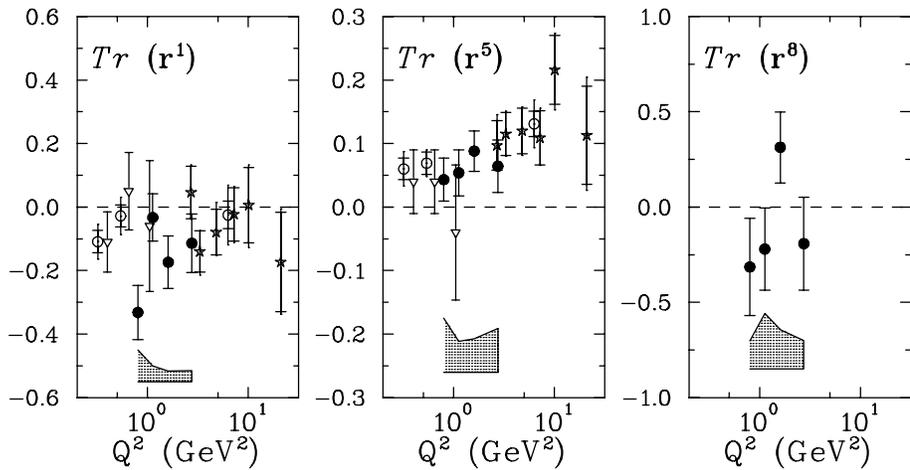

Fig. 14. The matrix elements $\mathrm{Tr}(r^1)$, $\mathrm{Tr}(r^5)$ and $\mathrm{Tr}(r^8)$, as a function of Q^2 ($\bullet$), with the band representing the systematic uncertainty. There are also shown previous measurements from H1 [11] ($\star$), and also values from DESY [1] ($\triangledown$) (with statistical uncertainties only) and ZEUS [10] ($\circ$), calculated from measurements of $r_{11}^{1,5}$ and $r_{00}^{1,5}$. Where the systematic uncertainties were specified [9,11], they are added in quadrature to produce the outer error bars.

$\langle Q^2 \rangle$ (GeV^2)	$\langle \epsilon \rangle$	$\mathrm{Tr}(r^1)$	$\mathrm{Tr}(r^5)$	$\mathrm{Tr}(r^8)$
0.80	0.76	$-0.332 \pm 0.085 \pm 0.100$	$0.043 \pm 0.034 \pm 0.085$	$-0.314 \pm 0.256 \pm 0.148$
1.13	0.82	$-0.033 \pm 0.075 \pm 0.049$	$0.054 \pm 0.036 \pm 0.048$	$-0.221 \pm 0.215 \pm 0.291$
1.60	0.81	$-0.174 \pm 0.083 \pm 0.033$	$0.088 \pm 0.032 \pm 0.052$	$0.314 \pm 0.186 \pm 0.206$
2.75	0.78	$-0.114 \pm 0.092 \pm 0.035$	$0.064 \pm 0.041 \pm 0.069$	$-0.192 \pm 0.243 \pm 0.150$

Table 4. Spin density matrix elements describing the production angle distributions $\mathcal{W}(\Phi)$. The first (second) uncertainty is statistical (systematic).

nisms are important at the energy and Q^2 accessible at HERMES.

The constraint $R(Q^2 = 0) = 0$ and the prediction by several models that the longitudinal and transverse cross sections should differ by some power of Q^2 [2,14,15] suggest a fit of the form

$$R(Q^2) = c_0(W) \left[\frac{Q^2}{M_\rho^2} \right]^{c_1}. \qquad (22)$$

The available data now span a wide range of centre-of-mass energies both above and below $W = 7\,\mathrm{GeV}$. This is close to the energy at which the W-dependence of the ρ^0 production cross section makes a transition from a decreasing behavior attributed to Reggeon exchange to a $W^{0.22}$ dependence attributed to Pomeron exchange. The improved precision that the present data add to the lower energy region allows the fit to be done with two values of

c_0 [42]: one for the data from high energy muon beams and collider experiments spanning $7 \lesssim W < 140\,\mathrm{GeV}$ (EMC [6], NMC [7], E665 [8], ZEUS [9], and H1 [11]), and another for the present data in the lower beam energy range $3.8 < W < 6.5\,\mathrm{GeV}$, yielding

$$c_0 = \begin{cases} 0.32 \pm 0.04, & 4 < \langle W \rangle < 7\ \mathrm{GeV} \\ 0.48 \pm 0.03, & \langle W \rangle > 7\ \mathrm{GeV} \end{cases}$$
$$c_1 = 0.66 \pm 0.03.$$

The χ^2 per degree of freedom for the combined fit is 20.7/20, calculated from the statistical uncertainties, plus the systematic uncertainties in quadrature where the latter are available. Difficulties in assessing the systematic uncertainties in some of the data sets preclude a comprehensive treatment of all the systematic uncertainties.

The only previous R data [12] in the HERMES energy region is consistent but insufficiently precise to influence
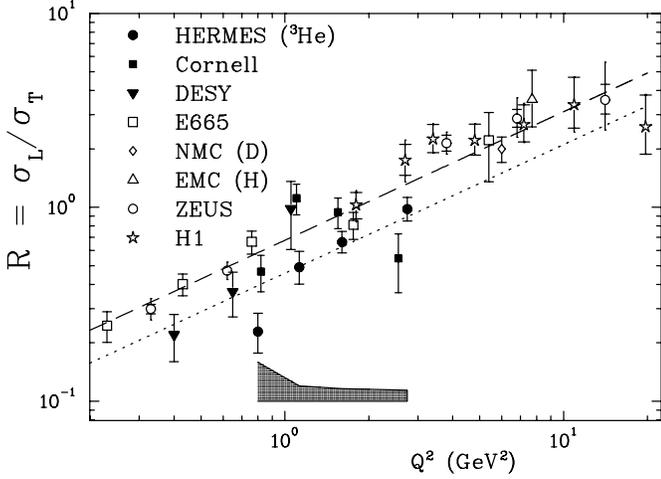
Fig. 15. The ratio $R \equiv \sigma_L/\sigma_T$ determined from the measured values of r_{00}^{04} using (21) ($\bullet$). The errors bars are statistical only, while the shaded region indicates the systematic uncertainty of the present data. Previous measurements are shown for comparison, with experiment names as in Fig. 10 with the addition of Cornell for ref. [4]. Where the systematic uncertainties were specified [9,11], they are added in quadrature to produce the outer error bars. The dashed (dotted) line represents a simultaneous fit according to (22) to data with average $W > 4$ and above (below) 7 GeV, which are shown as open (filled) data points. The DESY and Cornell data for $2 < W < 4\,\mathrm{GeV}$ are also plotted but were not included in the fit (see text).

Table 5. R as determined from r_{00}^{04}.

$\langle Q^2 \rangle$ (GeV^2)	$\langle \epsilon \rangle$	R
0.80	0.76	$0.23^{+0.06+0.15}_{-0.05-0.12}$
1.13	0.82	$0.49^{+0.10+0.10}_{-0.09-0.09}$
1.60	0.81	$0.66^{+0.09+0.11}_{-0.08-0.10}$
2.75	0.78	$0.98^{+0.15+0.14}_{-0.13-0.13}$

the fit. Inclusion of either or both of two existing data sets [1,4] in the range $2 < W < 4\,\mathrm{GeV}$ changes the results of the fit by less than one standard deviation, and does not significantly improve the precision. (It may be noted that the data of reference [4] are not well-described by the fit function — their χ^2 contribution would be similar to that of all of the rest of the fitted data in both energy regimes.)

As observed in previous experiments, the Q^2 dependence of R is in marked disagreement with the prediction of either VMD [42] or pQCD [15] that $c_1 \equiv 1$. The value of c_0 is found to increase with centre-of-mass energy in the range above $W = 4\,\mathrm{GeV}$ where both longitudinal and transverse production are clearly diffractive.[1] It has been shown [25] that the energy dependences of the lon-

gitudinal and transverse couplings for gluon exchange are identical, so that R is independent of energy at high energy; however, recent theoretical work [19] has suggested that at lower energy where quark exchange is dominant, there may be an additional class of diagrams that enhance the transverse couplings. The observed energy dependence of c_0 is consistent with this trend. However, it should be kept in mind that the lower energy fit to the present data set on the ^{3}He target could be influenced by nuclear effects, although it has been suggested that this would *increase R* [2]. Other matrix elements accessible with a real photon beam were found to be the same for coherent ρ^0 production on deuterium and incoherent production on either nucleon in deuterium [43]. Furthermore, those data are consistent with other similar measurements on hydrogen [44]. Finally, coherent production on such a light nucleus as ^{3}He accounts for only about 25% of the events (see Fig. 4). Hence a nuclear effect is unlikely to account for the observed difference from the results at higher energy.[2]

6 Summary

The production and decay-angle distributions for the combined coherent and incoherent polarized electroproduction of ρ^0 mesons from ^{3}He have been measured at photon virtuality $0.5 < Q^2 < 4\,\mathrm{GeV}^2$ and photon-nucleon centre-of-mass energy $3.8 < W < 6.5\,\mathrm{GeV}$. The spin-density matrix elements r_{00}^{04}, r_{1-1}^{04}, r_{1-1}^{1}, r_{1-1}^{3}, $\mathrm{Tr}\,(r^1)$, $\mathrm{Tr}\,(r^5)$ and $\mathrm{Tr}\,(r^8)$ are found to be mostly consistent with s-channel helicity conservation and natural parity exchange in the t-channel. Possible deviations from SCHC at the few sigma level were found for $\mathrm{Tr}(r^1)$. The ratio R of the cross sections for longitudinal and transverse photons was determined from the decay-angle distribution over a range $0.5 < Q^2 < 4\,\mathrm{GeV}^2$ and at $\langle W \rangle = 5\,\mathrm{GeV}$. The Q^2 dependence of R is consistent with previous experiments, exhibiting a monotonic increase with Q^2; however, the present data now suggest that at a given Q^2 value, R increases with average photon-nucleon centre-of-mass energy for such energies above $4\,\mathrm{GeV}$, assuming that nuclear effects in coherent production on ^{3}He can be neglected.

References

1. P. Joos *et al.*, Nucl. Phys. B **113** (1976) 53.
2. T.H. Bauer *et al.*, Rev. Mod. Phys. **50** (1978) 261.

---

[1] Experiments at lower energy [1,5] provide evidence that for fixed Q^2, R increases also as W falls below $2\,\mathrm{GeV}$.

[2] The distinction between coherent and incoherent processes can be better studied in a heavier nucleus such as ^{14}N. An analysis of such data is underway.

3. C. del Papa *et al.*, Phys. Rev. D **19** (1979) 1303.
4. D.G. Cassel *et al.*, Phys Rev. D **24** (1981) 2787.
5. CHIO Collab., W.D. Shambroom *et al.*, Phys. Rev. D **26** (1982) 1.
6. EMC, J.J. Aubert *et al.*, Phys. Lett. B **161** (1985) 203.
7. NMC, M. Arneodo *et al.*, Nucl. Phys. B **429** (1994) 503.
8. E665 Collab., M.R. Adams *et al.*, Z. Phys. C **74** (1997) 237.
9. ZEUS Collab., J. Breitweg *et al.*, Eur. Phys. J. C **6** (1999) 603.
10. ZEUS Collab., J. Breitweg *et al.*, Eur. Phys. J. C **12** (2000) 393.
11. H1 Collab., C. Adloff *et al.*, Eur. Phys. J. C **13** (2000) 371.
12. J.T. Dakin *et al.*, Phys. Rev. D **8** (1973) 687.
13. A. Donnachie and P.V. Landshoff, Z. Phys. C **2** (1979) 550.
14. M.A. Pichowsky and T.S.H. Lee, Phys. Lett. B **379** (1996) 1.
15. S.J. Brodsky *et al.*, Phys. Rev. D **50** (1994) 3134.
16. A. Donnachie and P.V. Landshoff, Nucl. Phys. B **311** (1989) 509; Phys. Lett. B **348** (1995) 213.
17. L.P.A. Haakman *et al.*, Phys. Lett. B **365** (1996) 411.
18. P.D.B. Collins, Phys. Rep. C **1** (1971) 103.
19. M. Vanderhaeghen, P.A.M. Guichon, and M. Guidal, Phys. Rev. Lett. **80** (1998) 5064; Phys. Rev. D **60** (1999) 094017.
20. H.G. Dosch *et al.*, Phys. Rev. D **55** (1997) 2602.
21. M.G. Ryskin, Z. Phys. C **57** (1993) 89.
22. M.G. Ryskin *et al.*, Z. Phys. C **76** (1997) 231.
23. K. Schilling and G. Wolf, Nucl. Phys. B **61** (1973) 381.
24. M.A. Pichowsky and T.S.H. Lee, Phys. Rev. D **56** (1997) 1644.
25. L. Frankfurt, W. Koepf and M. Strikman, Phys. Rev. D **54** (1996) 3194.
26. L. Mankiewicz, G. Piller and A. Radyushkin, Eur. Phys. J. C **10** (1999) 307;
    L. Mankiewicz, G. Piller and T. Weigl, Phys. Rev. D **59** (1999) 017501; Eur. Phys. J. C **5** (1998) 119.
27. S.V. Goloskokov, Phys. Lett. B **315** (1993) 459.
28. J. Klenner, A. Schäfer, W. Greiner, Z. Phys. A **352** (1995) 203.
29. HERMES Collab., K. Ackerstaff *et al.*, Nucl. Instr. and Meth. A **417** (1998) 230.
30. B. Povh and J. Hüfner, Phys. Rev. Lett. **58** (1987) 1612.
31. G. Ingelman, A. Edin, J. Rathsman, Comput. Phys. Commun. **101** (1997) 108.
32. Y. Akimov *et al.*, Phys. Rev. D **14** (1976) 3148.
33. H1 Collab., C. Adloff *et al.*, Z. Phys. C **75** (1997) 607.
34. M.G. Ryskin and Yu.M. Shabelski, Phys. Atom. Nucl. **61** (1998) 81.
35. J.A. Crittenden, Springer Tracts in Modern Physics **140** (1997).
36. J. Ballam *et al.*, Phys. Rev. D **5** (1972) 545.
37. V. Dmitrasinovic and F. Gross, Phys. Rev. C **40** (1989) 2479.
38. L.N. Hand, Phys. Rev. **129** (1963) 1834.
39. M. Ross and L. Stodolsky, Phys. Rev. **149** (1966) 1172.
40. M. Kolstein, Ph. D. Thesis, Vrije Universiteit, Amsterdam (1998), HERMES 98-046.
41. L.W. Mo and Y.S. Tsai, Rev. Mod. Phys. **41** (1969) 205.
42. J.J. Sakurai, Phys. Rev. Lett. **22** (1969) 981.
43. Y. Eisenburg *et al.*, Nucl. Phys. B **104** (1976) 61.
44. J. Ballam *et al.*, Phys. Rev. D **7** (1973) 3150.